A two-site Kitaev chain in a two-dimensional electron gas

ten Haaf, S.L.D.; Wang, Q.; Bozkurt, A.M.; Liu, C.; Kulesh, I.; Kim, Philip; Xiao, Di; Thomas, Candice; Manfra, Michael J.; Dvir, T.

DOI
10.1038/s41586-024-07434-9

Publication date
2024

Document Version
Final published version

Published in
Nature: international weekly journal of science

Citation (APA)
ten Haaf, S. L. D., Wang, Q., Bozkurt, A. M., Liu, C., Kulesh, I., Kim, P., Xiao, D., Thomas, C., Manfra, M. J., Dvir, T., Wimmer, M. T., & Goswami, S. (2024). A two-site Kitaev chain in a two-dimensional electron gas. *Nature: international weekly journal of science*, *630*(8016), 329-334. https://doi.org/10.1038/s41586-024-07434-9

Article

A two-site Kitaev chain in a two-dimensional electron gas

https://doi.org/10.1038/s41586-024-07434-9

Received: 18 November 2023

Accepted: 17 April 2024

Published online: 12 June 2024

Check for updates

Sebastiaan L. D. ten Haaf[1,5], Qingzhen Wang[1,5], A. Mert Bozkurt[1], Chun-Xiao Liu[1], Ivan Kulesh[1], Philip Kim[1], Di Xiao[2], Candice Thomas[2], Michael J. Manfra[2,3,4], Tom Dvir[1], Michael Wimmer[1] & Srijit Goswami[1]✉

Artificial Kitaev chains can be used to engineer Majorana bound states (MBSs) in superconductor–semiconductor hybrids[1–4]. In this work, we realize a two-site Kitaev chain in a two-dimensional electron gas by coupling two quantum dots through a region proximitized by a superconductor. We demonstrate systematic control over inter-dot couplings through in-plane rotations of the magnetic field and via electrostatic gating of the proximitized region. This allows us to tune the system to sweet spots in parameter space, where robust correlated zero-bias conductance peaks are observed in tunnelling spectroscopy. To study the extent of hybridization between localized MBSs, we probe the evolution of the energy spectrum with magnetic field and estimate the Majorana polarization, an important metric for Majorana-based qubits[5,6]. The implementation of a Kitaev chain on a scalable and flexible two-dimensional platform provides a realistic path towards more advanced experiments that require manipulation and readout of multiple MBSs.

Superconductor–semiconductor hybrid systems have been intensively investigated as a potential platform to engineer topologically protected Majorana bound states (MBSs). In particular, significant efforts have been dedicated to studying one-dimensional systems coupled to *s*-wave superconductors[7–9]. However, uncontrolled microscopic variations in hybrid devices have complicated the study of MBSs[10–12]. A potential way to mitigate the effects of disorder is to create a Kitaev chain[13] using an array of quantum dots (QDs) with controllable couplings[1–3]. In fact, a chain consisting of only two QDs, although not topologically protected, is sufficient to create localized MBSs[2]. These so-called poor man's Majoranas have recently been realized in nanowires[4], which has led to proposals[6,14–16] to study non-Abelian statistics by fusing or braiding MBSs in multiple two-site chains. However, to perform these studies and move towards a Majorana-based qubit with integrated readout and control, it is vital to have a scalable and flexible two-dimensional (2D) architecture.

In this work we realize a two-site Kitaev chain by coupling two spin-polarized QDs in an InSbAs 2D electron gas (2DEG). By tuning the couplings between the QDs to so-called sweet spots, we demonstrate correlated zero-bias conductance peaks (ZBPs) that are resilient to local perturbations. In addition to electrostatic control, we show that the planar 2DEG geometry allows one to reach such sweet spots through an in-plane rotation of the magnetic field. An important prerequisite to produce localized MBSs is that the Zeeman splitting in the QDs is sufficiently large[5]. Surprisingly, however, we find that several features used to identify 'sweet spots' (such as correlated ZBPs) actually persist down to zero magnetic field. We show that the evolution of the energy spectrum with magnetic field provides complementary information, which allows us to estimate the Majorana polarization, a metric quantifying the extent of hybridization between MBSs[5,6,17].

Model with strongly coupled dots

The Kitaev model[13] can be implemented by coupling spin-polarized QDs via Andreev bound states (ABSs) in a semiconductor–superconductor hybrid[4]. Coupling between the QDs is mediated by two types of coherent tunnelling processes, as illustrated in Fig. 1b. A hopping interaction arises through elastic co-tunnelling (ECT) and a pairing interaction arises via the creation or breaking of a Cooper pair in the superconductor through crossed Andreev reflection (CAR). To emulate a Kitaev chain, the relative amplitudes of these processes must be controlled[18–20]. Furthermore, large inter-dot couplings are desired to isolate zero-energy MBSs from higher-energy excitations[2]. This can be achieved by increasing tunnelling rates between the QDs and the proximitized region, additionally inducing superconducting correlations in the QDs[21,22]. In this regime the QDs can be described as Yu–Shiba–Rusinov (YSR) states[23–28].

An energy-level diagram of the system is shown in Fig. 1c, where, at finite magnetic field, the ground state of each proximitized QD is either a doublet state $|\downarrow\rangle$ or a singlet state $|S\rangle$. The electrochemical potential of the QDs are denoted μ_L and μ_R. We consider the combined state of the QDs $|\sigma_L, \sigma_R\rangle$, where $\sigma_L, \sigma_R \in (|S\rangle, |\downarrow\rangle)$. In this description, ECT and CAR processes give rise to two types of effective couplings. States with total odd parity ($|S, \downarrow\rangle$ and $|\downarrow, S\rangle$) have the same total spin ($\frac{1}{2}$) and therefore couple through a spin-conserving term Γ_o. States with total even-parity ($|S, S\rangle$ and $|\downarrow, \downarrow\rangle$) have different total spin (0 or 1) and couple through a spin non-conserving term Γ_e. Similar to a system with

[1]QuTech and Kavli Institute of NanoScience, Delft University of Technology, Delft, The Netherlands. [2]Department of Physics and Astronomy, Purdue University, West Lafayette, IN, USA. [3]Elmore School of Electrical and Computer Engineering, Purdue University, West Lafayette, IN, USA. [4]School of Materials Engineering, Purdue University, West Lafayette, IN, USA. [5]These authors contributed equally: Sebastiaan L. D. ten Haaf, Qingzhen Wang. ✉e-mail: s.goswami@tudelft.nl

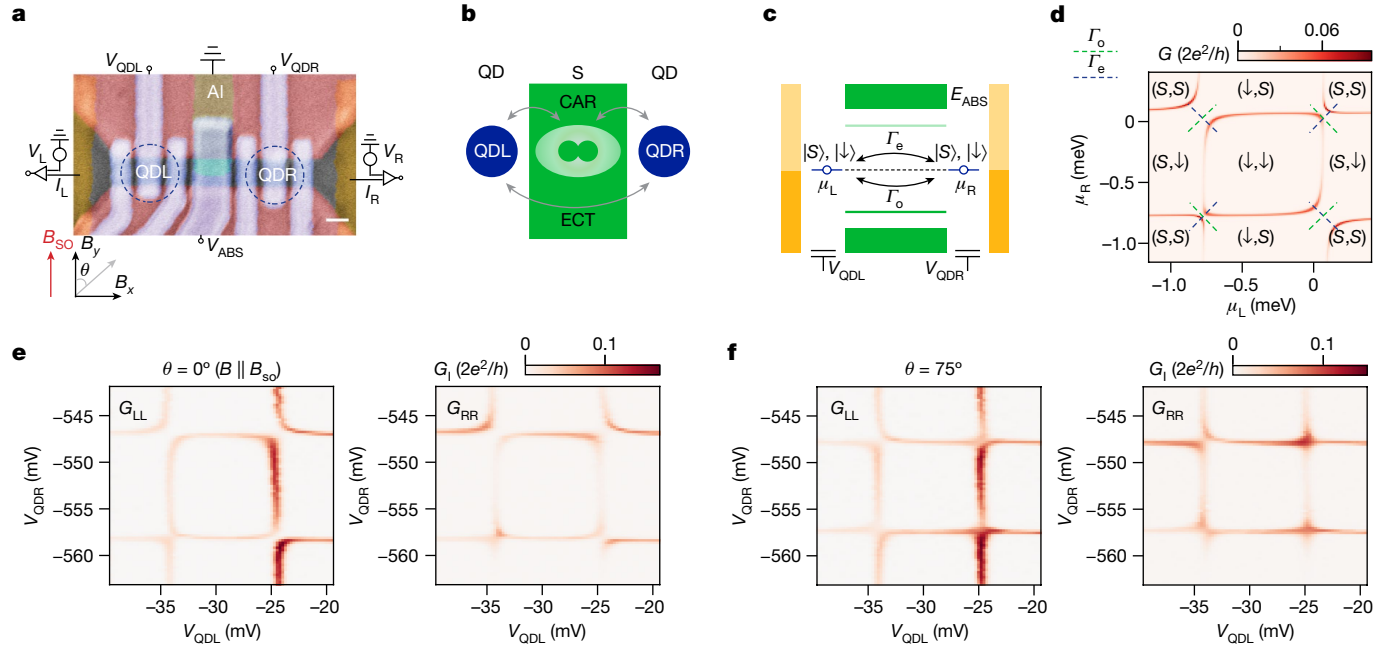

Fig. 1 | Device, model and CSDs. a, False-coloured scanning electron micrograph of device A. Inset axis shows coordinates of the external magnetic field and the expected spin–orbit field direction with respect to the device orientation. The gate-defined QDs (QDL and QDR) are indicated. Scale bar: 100 nm. **b**, Sub-gap transport processes between the QDs and the superconductor. ECT exchanges an electron between the QDs, while CAR allows for pairwise exchange of two electrons with the superconductor. **c**, Energy-level diagram showing two spin-polarized YSR states in two QDs that are coupled through a hybrid section. An Andreev bound state (at energy E_{ABS}) mediates two types of virtual tunnel couplings between the QDs, denoted by Γ_e and Γ_o. **d**, Numerically calculated CSD of two coupled QDs, in the absence of spin–orbit coupling. Dashed lines indicate which states are expected to be hybridized through each type of coupling. **e**, Measured CSD across two charge degeneracy points in QDL and QDR with $\theta = 0°$ ($\mathbf{B} \parallel \mathbf{B}_{SO}$), corresponding to the numerical conductance in **d**. **f**, Measured CSD with $\theta = 75°$. Data in **e** and **f** are taken at $V_{ABS} = -624$ mV and $B = 100$ mT.

non-proximitized QDs[1,2], MBSs should arise when these couplings are equal ($\Gamma_o = \Gamma_e$)[21], as further described in Methods. Figure 1d shows the numerically obtained conductance G, considering the local transport, as a function of μ_L and μ_R (details of the model can be found in Methods). This charge-stability diagram (CSD) reveals avoided crossings at the charge degeneracy points, indicative of strong inter-dot coupling. In the absence of spin–orbit interaction, only the spin-conserving coupling Γ_o is relevant, thus strongly hybridizing the odd-parity states. Horizontal and vertical conductance features are visible between avoided crossings as a result of local Andreev reflection, typical for YSR states.

Device description

A scanning electron micrograph of a typical device (device A) is shown in Fig. 1a. Gate-defined QDs are created on the left (QDL) and right (QDR) of a region proximitized by aluminium (green). The QDs are strongly coupled to the superconductor, resulting in the formation of sub-gap YSR states (detailed in Extended Data Fig. 1). Biases applied to the left and right leads (V_L and V_R) can be varied and the currents in the left and right leads (I_L and I_R) can be measured simultaneously. Using standard lock-in techniques, we measure local conductances $G_{LL}\left(\frac{dI_L}{dV_L}\right)$ and $G_{RR}\left(\frac{dI_R}{dV_R}\right)$, denoted G_l, and non-local conductances $G_{LR}\left(\frac{dI_L}{dV_R}\right)$ and $G_{RL}\left(\frac{dI_R}{dV_L}\right)$, denoted G_{nl}. We report on two similar devices. Device A was used for measurements in Figs. 1, 3 and 4. Device B (image shown in Extended Data Fig. 2a) was used to obtain the measurements in Fig. 2. All measurements are performed in a dilution refrigerator, with a base temperature of 20 mK.

By applying a magnetic field $\mathbf{B}$ along the spin–orbit field $\mathbf{B}_{SO}$, the effect of the spin–orbit interaction is suppressed (Extended Data Fig. 2), as previously observed in similar devices[29]. We measure G_l, as V_{QDL} and V_{QDR} are swept across two charge degeneracy points in each QD, resulting in the CSDs shown in Fig. 1e. Similar to the simulations (Fig. 1d), we find avoided crossings that indicate a strong coupling between odd-parity states, that is, $\Gamma_o > \Gamma_e$. Next, we rotate the external magnetic field away from the spin–orbit field, allowing spin non-conserving processes to occur. This is reflected in the avoided crossings in the CSDs (Fig. 1f), where we indeed see that even-parity states can now hybridize, indicating a sizeable Γ_e. In particular, the top-left and bottom-left avoided crossings have changed direction, indicating an even-parity ground state at these charge degeneracy points. The evolution from Fig. 1e,f suggests that the field angle can be used to tune the system into the sweet spot ($\Gamma_o = \Gamma_e$) where MBSs emerge.

Tuning to the Majorana sweet spot

We demonstrate this control in Fig. 2. Figure 2a shows a CSD obtained with $\mathbf{B} \perp \mathbf{B}_{SO}$, around the charge transition corresponding to the lower left corner of Fig. 1d. The diagonal avoided crossing here indicates that $\Gamma_e > \Gamma_o$. Rotating the field to align with $\mathbf{B}_{SO}$ results in an antidiagonal avoided crossing, as now $\Gamma_o > \Gamma_e$ (Fig. 2c). The separation between the branches of the avoided crossing is proportional to $\sqrt{|\Gamma_o^2 - \Gamma_e^2|}$ (detailed in Methods), which can be used to quantify the relative strength of the couplings. Measuring this quantity for several angles (Fig. 2d) shows a smooth evolution of the coupling strength as a function of the field angle. Importantly, at an intermediate angle the avoided crossing disappears (Fig. 2b), indicating $\Gamma_e = \Gamma_o$. Under these conditions, the odd- and even-parity ground states are degenerate at the charge degeneracy point, that is, $\delta\mu_L = \delta\mu_R = 0$, leading to localized MBSs on each QD[21]. We refer to this point in parameter space as the Majorana sweet spot. At the sweet spot, simultaneous tunnelling spectroscopy on the left and right QD demonstrates correlated ZBPs (Fig. 2e). Higher-energy excitations are visible at ±40 μV, providing an estimate of the effective

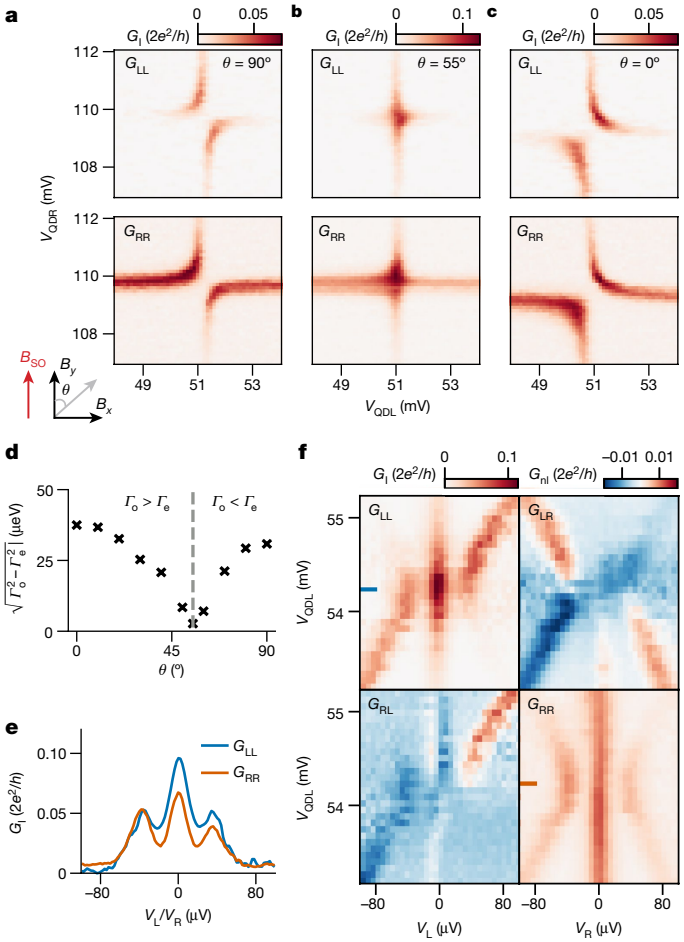

Fig. 2 | Tuning Γ_e and Γ_o with magnetic field angle. Measurements obtained for device B, characterized in Extended Data Fig. 2. **a**, CSD showing a diagonal avoided crossing ($\Gamma_e > \Gamma_o$), obtained with $\mathbf{B} \perp \mathbf{B}_{SO}$. **c**, Rotating the field such that $\mathbf{B} \| \mathbf{B}_{SO}$ the avoided crossing changes direction ($\Gamma_e < \Gamma_o$). **b**, At 55° the the avoided crossing disappears ($\Gamma_e = \Gamma_o$). **d**, Extraction of $\sqrt{|\Gamma_o^2 - \Gamma_e^2|}$ from CSDs measured at various magnetic field angles. **e**, G_I measured at the centre of the CSD in **b**, showing correlated zero-bias peaks. **f**, G_I and G_{nl} measured upon detuning V_{QDL} while keeping V_{QDR} on resonance. Correlated zero-bias peaks persist across a large voltage range. Raw data and the extraction procedure is presented in Extended Data Fig. 3. Measurements are taken at B = 80 mT.

couplings at the sweet spot to be $\Gamma_e = \Gamma_o \approx 20$ μeV. These ZBPs are expected to persist when only a single QD is perturbed, as they result from MBSs localized on each of the QDs. To confirm this, we measure G_I and G_{nl} upon detuning V_{QDL}, while keeping V_{QDR} constant (Fig. 2f). The ZBPs indeed persist in G_I, while higher-energy excitations are observed to disperse when QDL is detuned. Further, in G_{nl} only the higher-energy excitations are visible while the ZBPs themselves do not appear, a signature of the localized nature of these zero-energy states. These observations are consistent with experiments on nanowires[4] and theoretical predictions[2].

The above procedure for tuning to the sweet spot is guaranteed to work if one starts with a field angle where $\Gamma_e > \Gamma_o$, as Γ_e can always be decreased by rotating the field towards $\mathbf{B}_{SO}$. If a field rotation reveals that such an angle cannot be found, one can reach the sweet spot via electrostatic control over the hybrid section[4], as Γ_e and Γ_o are affected by the charge and energy of the ABSs[18,19]. In our devices the ABS energies are controlled by the voltage V_{ABS}, applied to the gate above the proximitized region. With the magnetic field directed away from the spin–orbit field (as in Fig. 1f), we study the evolution of the CSDs with V_{ABS}. Figure 3a shows a diagonal avoided crossing, signifying here that $\Gamma_o > \Gamma_e$. By tuning V_{ABS}, the avoided crossing changes direction, indicating $\Gamma_e > \Gamma_o$ (Fig. 3c). At an intermediate V_{ABS} the avoided crossing disappears (Fig. 3b), satisfying the sweet spot condition ($\Gamma_e = \Gamma_o$). Similar to Fig. 2, we now detune V_{QDR} along the blue dashed line in Fig. 3b and measure G_I, again finding correlated, persisting ZBPs (Fig. 3d). Line-cuts from Fig. 3d are shown in Fig. 3, giving an estimate of $\Gamma_e = \Gamma_o = 25$ μeV. When both QDs are detuned simultaneously, along the green dashed line in Fig. 3b, the correlated ZBPs disperse quadratically (Fig. 3e). This is expected for a two-site Kitaev chain, where the ZBPs are only protected from local perturbations[2]. An extended dataset and a comparison with numerical results is shown in Extended Data Fig. 5.

In addition to G_I, the non-local measurements in Fig. 3a–c can provide further information about underlying transport mechanisms. For example, it has been shown that for CAR, local and non-local signals have the same sign, whereas for ECT their sign should be opposite[20]. As charge is ill-defined for YSR states, there is no one-to-one correspondence between the dominant inter-dot coupling (that is, Γ_e, Γ_o) and the dominant underlying transport mechanism (that is, CAR, ECT). Nevertheless we find a qualitatively similar behaviour, whereby for $\Gamma_o > \Gamma_e$ the non-local conductance is positive, whereas for $\Gamma_e > \Gamma_o$ it is negative. We show that this is indeed expected (Extended Data Fig. 7), and that the sign of G_L is dictated by the positions of the QDs with respect to their charge degeneracy.

Majorana polarization

The ideal Kitaev chain is based on a spinless model. Thus, emulating this system with spinful QDs, as presented here, requires the Zeeman energies of the QDs to be sufficiently large compared to the effective coupling between the QDs[1–3,6,21]. In addition, MBSs on either QD should be isolated from each other. A parameter capturing these factors is the so-called Majorana polarization[17], which has recently been investigated theoretically in the context of Kitaev chains[5]. The Majorana polarization is a metric (denoted $|M|$) that quantifies the extent to which localized MBSs hybridize, and is relevant for experiments that require controlled manipulation of multiple MBSs, such as braiding[6,15] and parity-based qubits[2,14,30,31]. The Majorana polarization ranges from 0 (lowest polarization) to 1 (highest polarization), and in experiments it is desirable to have a high value of Majorana polarization. It was shown that both 'low' and 'high' Majorana polarization can result in similar transport signatures[5], raising an important question about how one could experimentally distinguish between these regimes.

To investigate this, we track the evolution of the system from 300 mT to 0 mT (along $\mathbf{B}_z$). At each field, we find similar crossings in the CSDs (Fig. 4a–c). Simultaneous tunnelling spectroscopy of the QDs at these crossing points reveal correlated ZBPs, down to zero magnetic field (Fig. 4d). Furthermore, the behaviour of non-local conductance around the centre of each crossing[5] also shows no discernible difference as the field is reduced. At first instance, these observations are surprising, as MBSs require time-reversal symmetry to be broken. However, we note that the combination of time-reversal symmetry and Coulomb interactions can result in robust zero-energy modes associated with Kramers pairs of Majorana zero modes, as discussed in ref. 32. While further investigation is needed to confirm this interpretation, we can conclude that experimentally it is difficult to extract information about the Majorana polarization from such measurements.

On the other hand, we find that the dispersion of higher-energy excitations in tunnelling spectroscopy has a distinctly different behaviour at each magnetic field, and allows us to obtain information about the Majorana polarization. While the ZBPs themselves persist upon detuning QDR for all values of B, the excited states show a markedly different behaviour (Fig. 4e–g). For example, at large detuning of QDR, excited states are visible at ±100 μV in Fig. 4e, while reaching

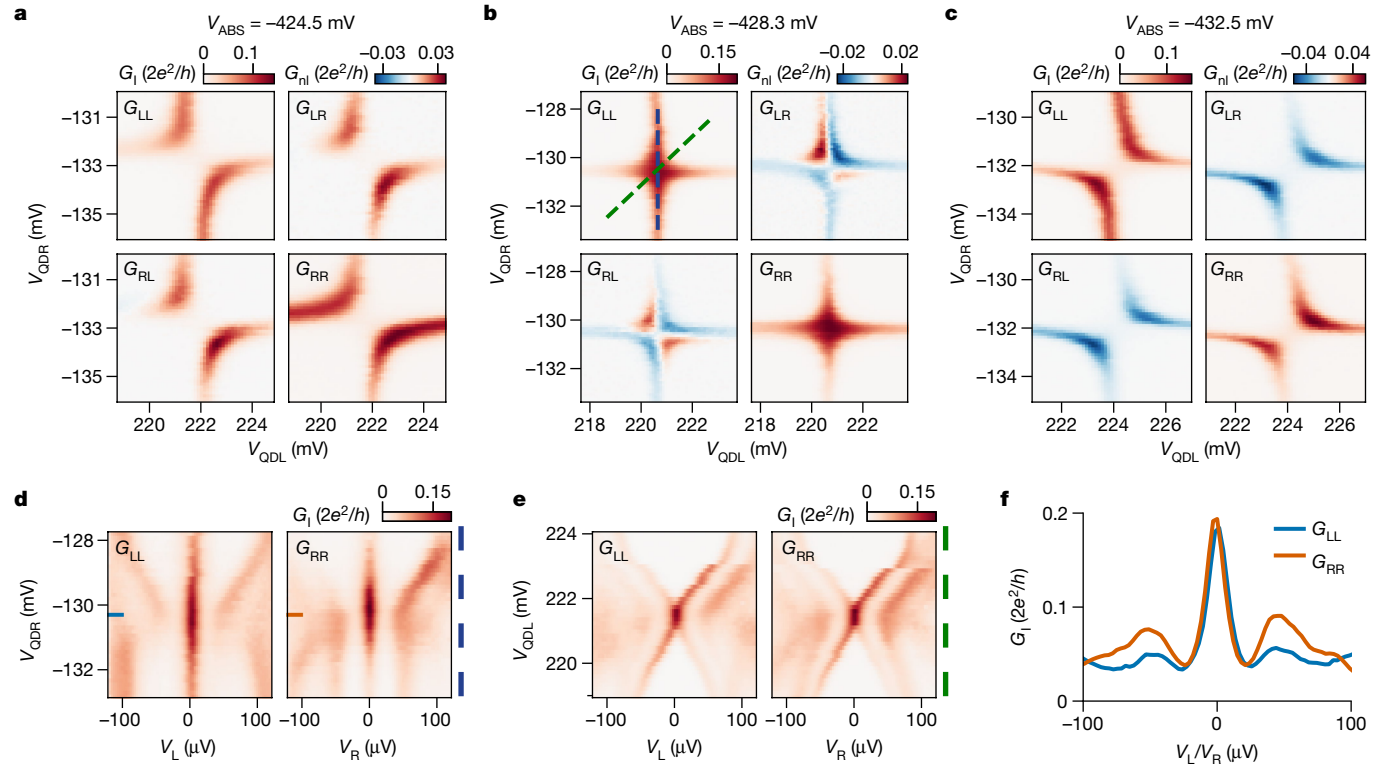

Fig. 3 | Electrostatically tuning to the Majorana sweet spot. a–**c**, CSDs taken at three different applied voltages V_{ABS} in device A. The system is smoothly tuned from the $\Gamma_o > \Gamma_e$ regime in **a** to the $\Gamma_o < \Gamma_e$ regime in **c**. In between, the $\Gamma_o = \Gamma_e$ condition is satisfied (**b**). A more extensive range is highlighted in Extended Data Fig. 6. **d**, Tunnelling spectroscopy measurements at the sweet spot. V_{QDR} is tuned along the blue path shown in **b**, while QDL is kept on resonance. **e**, Tunnelling spectroscopy as V_{QDL} and V_{QDR} are tuned simultaneously along the green path shown in **b**. **f**, Line-trace from **d** with V_{QDL} and V_{QDR} tuned to the sweet spot in **b** (corresponding to $\delta\mu_L = \delta\mu_R = 0$). Data is taken with $B = 150$ mT.

only ±60 μV in Fig. 4f. We denote this energy difference between the first excited states and the ZBPs as E_{gap} at the sweet spot and as E_{det} at large negative detuning, and extract these energies over an extensive range in B (Fig. 4h). Both E_{det} and E_{gap} are found to increase monotonically with increasing magnetic field. For these sets of measurements, E_{gap} starts to saturate at 30 μV at higher fields, while E_{det} increases linearly, saturating at 80 μV. The latter can be expected as the excitation energy of the hybrid system approaches the excitation energy, that is, the Zeeman energy (E_z) of an isolated QD, when either of the QDs is detuned.

We compare these measurements with numerical simulations of the system with input from experimental parameters, and find that indeed E_{det} provides a lower bound estimate of E_z of the QDs (Extended Data Fig. 8). This allows us to approximate a g-factor from Fig. 4h. Using this, the simulated spectra demonstrate a qualitatively similar behaviour in the dispersion of the excited states (Fig. 4i–k). Furthermore, we find that the evolution of both E_{gap} and E_{det} compare well to the experimental results (Fig. 4l).

These results allow us to numerically estimate the Majorana polarization for the system, as a function of magnetic field (Fig. 4l). We find that as B increases, the Majorana polarization increases quickly from 0 and then starts to approach 1 around 100 mT, where E_{gap} begins to saturate. The comparison here yields $|M| \approx 0.96$ at around $B = 300$ mT. A similar analysis is performed for measurements using the sweet spot shown in Fig. 3, where E_{gap} reaches 50 μV, from which we extract a lower Majorana polarization estimate of $|M| \approx 0.9$ (Extended Data Fig. 10). Whether these estimates can be considered a 'high' Majorana polarization depends on the operations one intends to perform. For example, specific braiding protocols have been shown to be reliable for $|M| = 0.98$ (ref. 6). It should be noted that these experiments do not constitute a direct measurement of the Majorana polarization. One way to achieve this would be to introduce an additional QD on either side, with a tunnelling coupling to either MBS[32–34]. Regardless, the presented measurements show that the evolution of the system from zero magnetic field to high magnetic field can be well understood within the framework of the Kitaev model.

Conclusion

In summary, we have implemented a two-site Kitaev chain in a 2DEG by coupling QDs through ABSs in a superconductor–semiconductor hybrid region. We demonstrate a smooth control over the inter-dot couplings, both by rotations of the magnetic field and by tuning of the energy of Andreev bound states in the hybrid section. At specific points in the parameter space, zero-energy excitations arise that are stable against local perturbations of either QD. We show that these 'sweet spots' (accompanied by correlated ZBPs) appear in the system even at zero Zeeman energy, and are by themselves insufficient to gain information about the polarization of MBSs. Rather, we find that the magnetic field dependence of the energy spectrum allows us to distinguish between high and low polarization regimes. Our work demonstrates that artificial Kitaev chains can now be realized on a scalable and flexible platform, and that 2DEGs are poised to perform Majorana-based experiments that were previously inaccessible.

Online content

Any methods, additional references, Nature Portfolio reporting summaries, source data, extended data, supplementary information, acknowledgements, peer review information; details of author contributions

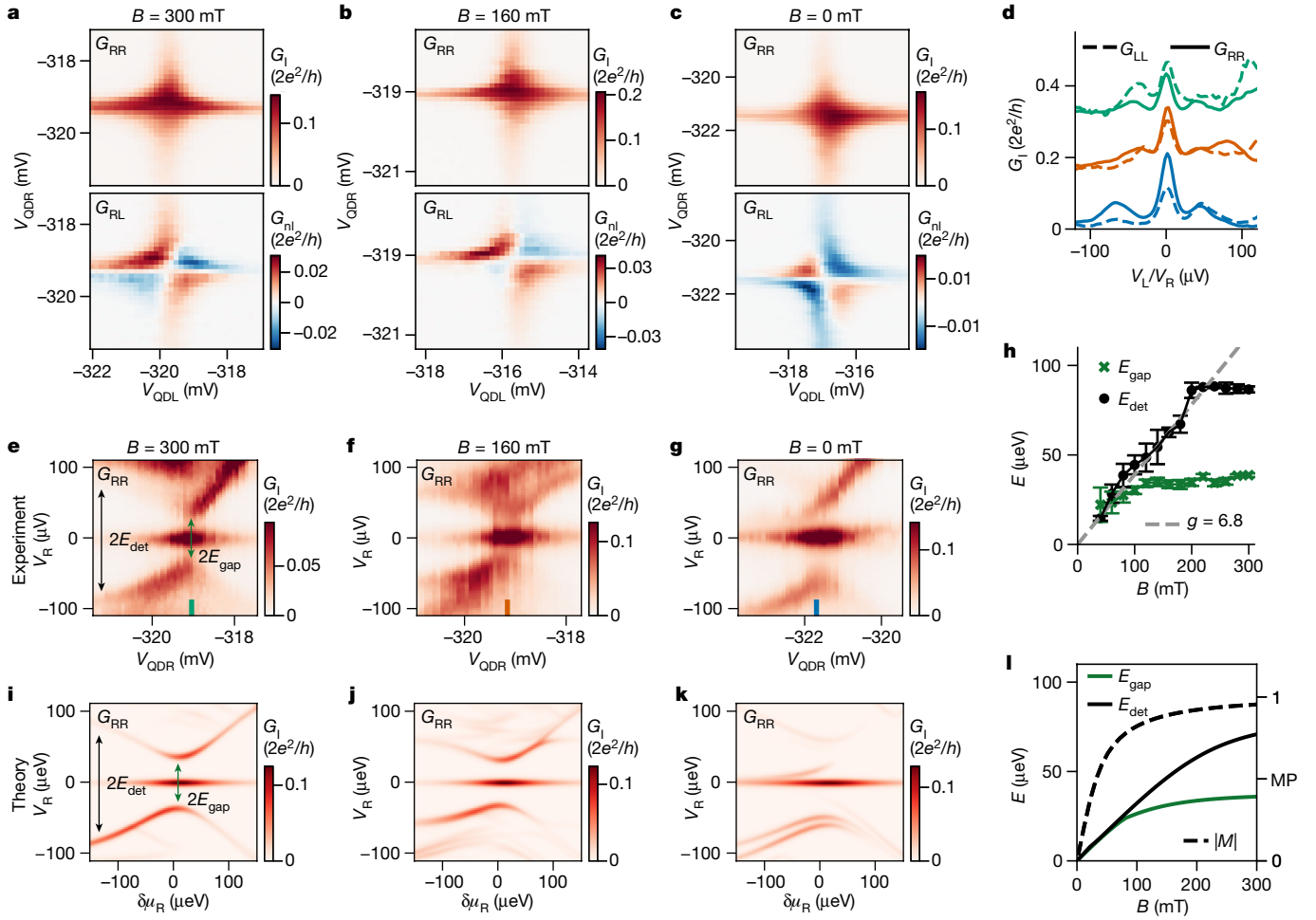

Fig. 4 | Majorana sweet spots in varying magnetic field. a–**c**, CSDs at Majorana sweet spots measured at applied fields of 300 mT (**a**), 160 mT (**b**) and 0 mT (**c**). At each field, V_{ABS} is adjusted to tune to the sweet spot, following the procedure from Fig. 3. **d**, G_{RR} (solid) and G_{LL} (dashed) line-cuts at the centre of each CSD, from indicated positions in **e**–**g**, highlighting the presence of correlated ZBPs. Offsets of 0.15 and 0.3 are applied for 160 mT and 300 mT respectively. **e**–**g**, Measured G_{RR} upon detuning QDR, while keeping QDL on resonance. Data is saturated for visibility of the excited states. Energies of interest (E_{gap} and E_{det}) are highlighted in **e**. **h**, Extraction of the energies E_{gap} and E_{det} from measurements between 300 mT and 0 mT (full dataset in Extended Data Fig. 9). Dashed line shows a linear fit of E_{det}, providing an estimate for the g-factor of QDL. **i**–**k**, Numerically calculated conductance at the field values indicated in **e**–**g** respectively. **l**, Numerically extracted evolution of E_{gap} and E_{det} (solid) and corresponding Majorana polarization $|M|$ (dashed) as a function of the magnetic field.

and competing interests; and statements of data and code availability are available at https://doi.org/10.1038/s41586-024-07434-9.

1. Sau, J. D. & Sarma, S. D. Realizing a robust practical Majorana chain in a quantum-dot-superconductor linear array. *Nat. Commun.* **3**, 964 (2012).
2. Leijnse, M. & Flensberg, K. Parity qubits and poor man's Majorana bound states in double quantum dots. *Phys. Rev. B* **86**, 134528 (2012).
3. Fulga, I. C., Haim, A., Akhmerov, A. R. & Oreg, Y. Adaptive tuning of Majorana fermions in a quantum dot chain. *New J. Phys.* **15**, 045020 (2013).
4. Dvir, T. et al. Realization of a minimal Kitaev chain in coupled quantum dots. *Nature* **614**, 445 (2023).
5. Tsintzis, A., Souto, R. S. & Leijnse, M. Creating and detecting poor man's Majorana bound states in interacting quantum dots. *Phys. Rev. B* **106**, L201404 (2022).
6. Tsintzis, A., Souto, R. S., Flensberg, K., Danon, J. & Leijnse, M. Majorana qubits and non-abelian physics in quantum dot–based minimal Kitaev chains. *PRX Quantum* **5**, 010323 (2024).
7. Lutchyn, R. M., Sau, J. D. & Das Sarma, S. Majorana fermions and a topological phase transition in semiconductor–superconductor heterostructures. *Phys. Rev. Lett.* **105**, 077001 (2010).
8. Oreg, Y., Refael, G. & von Oppen, F. Helical liquids and Majorana bound states in quantum wires. *Phys. Rev. Lett.* **105**, 177002 (2010).
9. Prada, E. et al. From Andreev to Majorana bound states in hybrid superconductor–semiconductor nanowires. *Nat. Rev. Phys.* **2**, 575 (2020).
10. Liu, C.-X., Sau, J. D., Stanescu, T. D. & Das Sarma, S. Andreev bound states versus Majorana bound states in quantum dot-nanowire-superconductor hybrid structures: trivial versus topological zero-bias conductance peaks. *Phys. Rev. B* **96**, 075161 (2017).
11. Vuik, A., Nijholt, B., Akhmerov, A. R. & Wimmer, M. Reproducing topological properties with quasi-Majorana states. *SciPost Phys.* **7**, 061 (2019).
12. Pan, H. & Das Sarma, S. Physical mechanisms for zero-bias conductance peaks in Majorana nanowires. *Phys. Rev. Res.* **2**, 013377 (2020).
13. Kitaev, A. Y. Unpaired Majorana fermions in quantum wires. *Physics-Usphekhi* **44**, 131 (2001).
14. Széchenyi, G. & Pályi, A. Parity-to-charge conversion for readout of topological Majorana qubits. *Phys. Rev. B* **101**, 235441 (2020).
15. Boross, P. & Pályi, A. Braiding-based quantum control of a Majorana qubit built from quantum dots. *Phys. Rev. B* **109**, 125410 (2024).
16. Liu, C.-X., Pan, H., Setiawan, F., Wimmer, M. & Sau, J. D. Fusion protocol for Majorana modes in coupled quantum dots. *Phys. Rev. B* **108**, 085437 (2023).
17. Sedlmayr, N. & Bena, C. Visualizing Majorana bound states in one and two dimensions using the generalized Majorana polarization. *Phys. Rev. B* **92**, 115115 (2015).
18. Liu, C.-X., Wang, G., Dvir, T. & Wimmer, M. Tunable superconducting coupling of quantum dots via Andreev bound states in semiconductor–superconductor nanowires. *Phys. Rev. Lett.* **129**, 267701 (2022).
19. Bordin, A. et al. Tunable crossed Andreev reflection and elastic cotunneling in hybrid nanowires. *Phys. Rev. X* **13**, 031031 (2023).
20. Wang, G. et al. Singlet and triplet Cooper pair splitting in hybrid superconducting nanowires. *Nature* **612**, 448 (2022).
21. Liu, C.-X. et al. Enhancing the excitation gap of a quantum-dot-based Kitaev chain. Preprint at https://arxiv.org/abs/2310.09106 (2023).
22. Zatelli, F. et al. Robust poor man's Majorana zero modes using Yu-Shiba-Rusinov states. Preprint at https://arxiv.org/abs/2311.03193 (2023).
23. Meng, T., Florens, S. & Simon, P. Self-consistent description of Andreev bound states in Josephson quantum dot devices. *Phys. Rev. B* **79**, 224521 (2009).

24. Grove-Rasmussen, K. et al. Superconductivity-enhanced bias spectroscopy in carbon nanotube quantum dots. *Phys. Rev. B* **79**, 134518 (2009).
25. Deacon, R. S. et al. Tunneling spectroscopy of Andreev energy levels in a quantum dot coupled to a superconductor. *Phys. Rev. Lett.* **104**, 076805 (2010).
26. Lee, E. J. et al. Spin-resolved Andreev levels and parity crossings in hybrid superconductor–semiconductor nanostructures. *Nat. Nanotechnol.* **9**, 79 (2014).
27. Jellinggaard, A., Grove-Rasmussen, K., Madsen, M. H. & Nygård, J. Tuning Yu-Shiba-Rusinov states in a quantum dot. *Phys. Rev. B* **94**, 064520 (2016).
28. Grove-Rasmussen, K. et al. Yu-Shiba-Rusinov screening of spins in double quantum dots. *Nat. Commun.* **9**, 2376 (2018).
29. Wang, Q. et al. Triplet correlations in Cooper pair splitters realized in a two-dimensional electron gas. *Nat. Commun.* **14**, 4876 (2023).
30. Dai, L., Kuo, W. & Chung, M.-C. Extracting entangled qubits from Majorana fermions in quantum dot chains through the measurement of parity. *Sci. Rep.* **5**, 11188 (2015).
31. Pino, D. M., Souto, R. S. & Aguado, R. Minimal Kitaev-transmon qubit based on double quantum dots. *Phys. Rev. B* **109**, 075101 (2024).
32. Clarke, D. J. Experimentally accessible topological quality factor for wires with zero energy modes. *Phys. Rev. B* **96**, 201109 (2017).
33. Prada, E., Aguado, R. & San-Jose, P. Measuring Majorana nonlocality and spin structure with a quantum dot. *Phys. Rev. B* **96**, 085418 (2017).
34. Souto, R. S., Tsintzis, A., Leijnse, M. & Danon, J. Probing Majorana localization in minimal Kitaev chains through a quantum dot. *Phys. Rev. Res.* **5**, 043182 (2023).

Methods

Device fabrication and yield

All devices were fabricated using techniques described in detail in ref. 35. A narrow aluminium strip is defined in an InSbAs–Al chip by wet etching, followed by the deposition of two normal Ti/Pd contacts. After deposition of 20 nm AlOx via atomic layer deposition, two Ti/Pd depletion gates are evaporated. Following a second atomic layer deposition layer (20 nm AlOx), seven Ti/Pd finger gates are evaporated to define the QDs and tune the ABSs' energy. The two depletion gates define a quasi-1D channel with a width of about 160 nm, contacted on each side by a normal lead. The aluminium strip induces superconductivity in the middle section of each device, with an induced gap on the order of 200 μeV. The presence of extended ABSs is confirmed through tunnelling spectroscopy. ABSs are found to be present over a large range of V_{ABS}, the voltage applied to the gate covering the hybrid region. Finger gates on the left and right of the aluminium define QDs with charging energies above 1 mV (Extended Data Fig. 1a,b).

Two devices were used to obtain the data presented in the main text (device A and device B). Both showed strong hybridization between the QDs, as presented here. Device A was used to study the field evolution of Majorana sweet spots and to obtain the measurements presented in Figs. 1, 3 and 4. Device B was used to demonstrate the role of spin–orbit coupling on the inter-dot interactions and the control over interactions through magnetic field as presented in Fig. 2. Regarding device yield, up until now we have measured 12 devices for the purpose of studying hybridized QDs. Of these, we could tune eight devices to regimes with strongly coupled QDs that showed the tunability displayed in Fig. 3. Of the non-functional devices, two failed due to trivial reasons (for example, losing electronic connection due to missing bondwires after cooling). The remaining two devices failed at the stage of forming the 1D channel, where we found some optimization was needed to discover the optimal separation between the top and bottom depletion gates.

Transport measurements and data processing

Measurements were performed in a dilution refrigerator with a base temperature of 20 mK. Transport measurements were performed in a.c. and d.c. using a three-terminal set-up, where the aluminium was electrically grounded. Each Ohmic lead was connected to a current-to-voltage converter and biased through a digital-to-analogue converter that applied both d.c. and a.c. biases. Offsets of the applied voltage-bias on each side were corrected via independent calibration of the Coulomb peaks in the QDs on each side. The voltage outputs of the current meters were recorded with two digital multimeters and two lock-in amplifiers. When a d.c. voltage was applied to the left Ohmic (V_L) the right lead (V_R) was kept grounded and vice versa. a.c. excitations were applied on each side with amplitudes of around 5 μV RMS and frequencies of 19 Hz (left) and 29 Hz (right). In this way, we measured the full conductance matrix G by first measuring the response of I_L and I_R to V_L and then to V_R. We accounted for the voltage-divider effect by correcting the conductances using known fridge line resistances (3.6 kΩ in device A, 3.3 kΩ in device B), as detailed in ref. 36. This correction was done for all presented spectroscopy data, except for the data shown in Fig. 3d–f. Magnetic fields were applied using a 3D vector magnet. The alignment of the magnetic field of device A is expected to be accurate to within ±10° and calibrated through performing tunnelling spectroscopy of the hybrid section as a function of field angle. The alignment of device B is expected to be accurate to within ±5°.

Due to device instabilities or charge jumps, the electrostatics of the QDs experience small drifts over the course of the measurements. Investigated orbitals were tracked while collecting the presented datasets. For each tunnelling spectroscopy measurements at a sweet spot, where V_{QDL} and/or V_{QDR} were detuned, a CSD was obtained directly before and directly after to ensure that no drifts occurred during such a measurement. If such a drift occurred, the measurement was discarded and repeated. Such drifts are the cause of small discrepancies in gate voltages between highlighted paths in Fig. 3b and the measurements shown in Fig. 3d,e. The highlighted path represents the corrected path taken with respect to the CSD shown in Fig. 3b, based on the CSDs obtained before and after the measurements.

Extracting QD parameters

To compare energy scales between experiments and numerical calculations, the gate voltages V_{QDL} and V_{QDR} are converted to electrochemical potential energies μ_L and μ_R. For this purpose we extract the dimensionless lever arms α. When forming sub-gap YSR states in the QDs, the effective lever arm of each QD around a zero-bias charge degeneracy can differ from the lever arm of the uncoupled QD, depending, for example, on hybridization with the hybrid region (Extended Data Fig. 4), extensively addressed in ref. 22. For analysis we therefore estimate both the normal-state lever arm (denoted α_N) and the lever arms of the sub-gap YSR states (denoted α_{YSR}) at the specific V_{ABS} regimes of interest. Device B was operated in a regime without significant difference between α_N and α_{YSR}, such that the analysis in Fig. 2d used the lever arms extracted in Extended Data Fig. 2. With the orbitals in Fig. 4, sweet spots were investigated at magnetic field values between 0 mT and 300 mT, where the energy of excited states E_{det} was extracted at a fixed detuning of V_{QDR}. A g-factor is extracted from this data, by a linear fit of E_{det} up to 180 mT (before saturation). For this dataset α_{YSR} was only obtained at 0 mT (Extended Data Fig. 1), such that any change in α_{YSR} as a function of magnetic field cannot be accounted for in the analysis in Fig. 4h. When extracting E_{det} at constant detuning of V_{QDR} at each field, μ_R may not be constant but rather is expected to decrease (Extended Data Fig. 4). We note that the lack of this correction may lead to a slight underestimation of the g-factor in Fig. 4h, which in turn will lead to a lowered estimation of the Majorana polarization. For the extractions of E_{det} and E_{gap}, G_{LL} and G_{RR} line-traces are obtained at the sweet spot and at a detuning of V_{QDR} of −2 mV, corresponding to a detuning of $\mu_R \approx 100$ μeV. From each line-trace, the separation between the ZBPs and the first higher-energy excitation is extracted by fitting Gaussian peaks symmetrically around zero bias. Error bars are given by the uncertainty in these fits.

Numerical transport calculations

For all presented numerical results, a description of the system incorporating both the two QDs and the middle hybrid section was used, recently introduced in ref. 5. We employ the same model and highlight key points, using the numerical parameter below. The model considers tunnelling between two normal QDs (L, R) and a central QD (M), which is in proximity to a superconductor. Each site j has electrochemical potential energy μ_j. A spin-conserving hopping t allows transport between the outer QDs and central QD. The effect of spin–orbit interactions is included through a spin-flip hopping term t_{SO} between the outer QDs and central QD. The presence of the superconductor is included by attributing a superconducting pairing term Δ_i in each QD. To match the experimental geometry, $\Delta_{L,R} < \Delta_M$. Lastly, the left and right sites are assigned a large on-site charging energy U and a Zeeman splitting E_z between the $|\downarrow\rangle$ and $|\uparrow\rangle$ occupation. The Hamiltonian is constructed as follows:

$$
\begin{aligned}
H = & \sum_{j,\sigma} \mu_j n_{j\sigma} + \sum_j U_j n_{j\uparrow} n_{j\downarrow} + \sum_j E_{Zj}(n_{j\downarrow} - n_{j\uparrow}) \\
& + \sum_{j\neq M,\sigma} [t_j d^\dagger_{j\sigma} d_{C\sigma} + h.c.] \\
& + \sum_{j\neq M} [t^{SO}_j d^\dagger_{j\downarrow} d_{C\uparrow} - t^{SO}_j d^\dagger_{j\uparrow} d_{C\downarrow} + h.c.] \\
& + \sum_j [\Delta_j d^\dagger_{j\uparrow} d^\dagger_{j\downarrow} + h.c.]
\end{aligned}
$$

where $d_{j\sigma}$, $d^{\dagger}_{j\sigma}$ and $n_{j\sigma}$ are the annihilation, creation and number operators respectively for each site. The sum j runs over the sites (L, M, R) and σ over the spin degree of freedom (↑, ↓). For simplicity, a left and right symmetry is assumed, such that a Majorana sweet spot lies along $\mu_L = \mu_R$. Sweet spots are obtained by scanning the parameter space spanned by $\mu_L = \mu_R$ and μ_M and finding degeneracies between the lowest odd and even eigenstates. All transport calculations are obtained using the rate equation detailed in ref. 5. Similar to ref. 5, we calculate the quantity of Majorana polarization (originally introduced in ref. 17). This quantity, denoted M_j, is defined per site j as:

$$M_j = \frac{\sum_\sigma (w_\sigma^2 - z_\sigma^2)}{\sum_\sigma (w_\sigma^2 + z_\sigma^2)}$$
$$w_\sigma = \langle O|(d_{j\sigma} + d^{\dagger}_{j\sigma})|E\rangle$$
$$z_\sigma = \langle O|(d_{j\sigma} - d^{\dagger}_{j\sigma})|E\rangle$$

where $|O\rangle$ and $|E\rangle$ are the lowest-energy odd and even states respectively. Due to symmetrically chosen parameters $|M_L| = |M_R| = |M|$, such that a single Majorana polarization value can be extracted for a specific set of parameters. To provide an experimental observable that reflects a high or low $|M|$, we investigate the behaviour of two transition energies, denoted as E_{gap} and E_{det}. Numerically these are obtained from the Hamiltonian as the energy difference between the lowest even state and the second-lowest odd state, at specific values of μ_L and μ_R. E_{gap} is obtained with μ_L and μ_R set to correspond to their sweet spot value. E_{det} is obtained with μ_R detuned by $\approx \Delta_M$. In the absence of the Zeeman term, both E_{gap} and E_{det} are zero by definition, due to the degeneracy of the odd states in the presence of time-reversal symmetry. The dependence of M, E_{gap} and E_{det} on E_z is demonstrated in Extended Data Fig. 10.

To compare to experiments, parameters are selected to match realistic values. We set $\Delta_M = 100$ μeV and $\Delta_{L,R} = 0.5\Delta_M$. The charging energy U is fixed in both dots to be $10\Delta_M$, except for Fig. 1d where a value of $7\Delta_M$ is used to better highlight the behaviour of all four avoided crossings in the large CSD. For the analysis in Fig. 4, tunnelling terms t and t_{SO} are fine-tuned such that at large E_z the sweet spot gap of 30 μeV is obtained, to match the experimental result. This gives $t_{SO} = 0.4t = 0.7\Delta_M$. Similarly, to compare to the experimental results in Extended Data Figs. 5 and 10, t and t_{SO} are fine-tuned to obtain a sweet spot gap of 50 μeV at large E_z. This results in $t_{SO} = 0.4t = 0.85\Delta_M$.

Effective model in the strong coupling regime

The above description is used for all presented calculations. To provide an intuitive understanding of these results, we invoke a description of the system through an effective model, introduced in detail in ref. 21. Here we provide a brief summary of the relevant findings. When the energy E_{ABS} of the sub-gap state in the middle site is large compared to tunnel couplings between the QDs, the middle site can be integrated out. This leaves a description of the system including only effective couplings between YSR states in the left and right QD sites. Additionally, it is assumed that E_z is sufficiently large such that only the $|\downarrow|$ occupation of each QD partakes in transport. In this description, a Hamiltonian can be constructed on a singlet–doublet basis. The ground state of each QD is either the $|\downarrow\rangle$ doublet or a singlet $|S\rangle$ of the form $|S\rangle = u_{L,R}|0\rangle - v_{L,R}|\downarrow\uparrow\rangle$. Here the u, v components depend on the chemical potential energies μ_L and μ_R of the left and right dot: $(u^2_{L,R} = 1 - v^2_{L,R} = \frac{1}{2} + \frac{\mu_{L,R} + U}{\sqrt{U^2 + E^2_{ABS}}})$. The effective Hamiltonian is obtained:

$$H^{\text{eff}}_{\text{coupling}} = \sum_{\sigma,\eta=\uparrow,\downarrow} (t_{\sigma\eta} c^{\dagger}_{L\sigma} c_{R\eta} + \Delta_{\sigma\eta} c^{\dagger}_{L\sigma} c^{\dagger}_{R\eta}) + h.c., \quad (1)$$

where $c_{L,R}$ and $c^{\dagger}_{L,R}$ are annihilation and creation operators for the left and right sites. Further, $t_{\sigma\eta}$ specifies the amplitude of an electron with spin σ from left site tunnelling to occupy a state with spin η in the right side, or vice versa. $\Delta_{\sigma\mu}$ specifies the amplitude of the creating or breaking of a Cooper pair through electrons with spins σ and η in the left and right QDs ($\sigma, \eta \in [\uparrow, \downarrow]$). Due to the spin–orbit interaction two equal-spin electrons can also be coupled via the Δ term. Importantly, this description is equivalent to the weakly coupled model discussed in ref. 2, when changing from a charge occupation basis to a YSR-state basis. Now, two types of coupling arise between the total even-parity states (denoted Γ_E) and between total odd-parity states (Γ_O). Each are a combination of ECT and CAR amplitudes:

$$\Gamma_E = \langle SS|H^{\text{eff}}_{\text{coupling}}|\downarrow\downarrow\rangle$$
$$= -\Delta_{\uparrow\uparrow} v_L v_R + \Delta_{\downarrow\downarrow} u_L u_R + t_{\uparrow\downarrow} v_L u_R - t_{\downarrow\uparrow} u_L v_R,$$
$$\Gamma_O = \langle S\downarrow|H^{\text{eff}}_{\text{coupling}}|\downarrow S\rangle$$
$$= -t_{\uparrow\uparrow} v_L v_R + t_{\downarrow\downarrow} u_L u_R + \Delta_{\uparrow\downarrow} v_L u_R - \Delta_{\downarrow\uparrow} u_L v_R,$$

The coupling Γ_O results in bonding and anti-bonding states of the form $u|S,\downarrow\rangle \pm v|\downarrow, S\rangle$. Γ_E forms bonding and anti-bonding states of the form $\alpha|S, S\rangle \pm \beta|\downarrow,\downarrow\rangle$. When $\Gamma_E = \Gamma_O$ the even and odd ground states become degenerate at $\mu_L = \mu_R$, equivalent to the $t = \Delta$ condition in the "poor man's Majorana" description[2]. In Fig. 2d, we extract the distance between the branches of the avoided crossing in the experimentally obtained CSDs, after converting the gate voltages to the YSR energies of each QD. In the effective description this distance corresponds to analysing where the line $\mu_L = \mu_R$ or $\mu_L = -\mu_R$ intersects a degeneracy between the even and odd ground state energies. This gives two points, separated by $\sqrt{8|\Gamma_O^2 - \Gamma_E^2|}$.

Data availability

Raw data and analysis scripts for all presented figures are available via Zenodo at https://doi.org/10.5281/zenodo.10801215 (ref. 37).

35. Möhle, C. M. et al. Controlling Andreev bound states with the magnetic vector potential. *Nano Lett.* **22**, 8601 (2022).
36. Martinez, E. A. et al. Measurement circuit effects in three-terminal electrical transport measurements. Preprint at https://arxiv.org/abs/2104.02671 (2021).
37. ten Haaf, S. L. D. Data and code for "A two-site Kitaev chain in a two-dimensional electron gas". *Zenodo* https://doi.org/10.5281/zenodo.10801215 (2024).

Acknowledgements We thank M. Leijnse, G. Katsaros, G. Wang, N. van Loo, A. Bordin and F. Zatelli for valuable discussions and for providing comments on the manuscript. The experimental research at Delft was supported by the Dutch National Science Foundation (NWO) and a TKI grant of the Dutch Topsectoren Program. A.M.B. acknowledges NWO (HOTNANO) for their research funding. C.-X.L. acknowledges subsidy by the Top consortium for Knowledge and Innovation programme (TKI). S.G. and M.W. acknowledge financial support from the Horizon Europe Framework Program of the European Commission through the European Innovation Council Pathfinder grant no. 101115315 (QuKiT).

Author contributions S.L.D.t.H. fabricated the devices. Q.W. and I.K. contributed to the device design and optimization of fabrication flow. Measurements were performed by S.L.D.t.H., Q.W. and P.K. Numerical analysis was provided by S.L.D.t.H., A.M.B. and C.-X.L, under the supervision of M.W. MBE growth of the semiconductor heterostructures and the characterization of the materials was performed by D.X. and C.T. under the supervision of M.J.M. The manuscript was written by S.L.D.t.H., Q.W. and S.G., with inputs from all coauthors. T.D. and S.G. supervised the experimental work in Delft.

Competing interests The authors declare no competing interests.

Additional information
Supplementary information The online version contains supplementary material available at https://doi.org/10.1038/s41586-024-07434-9.

Correspondence and requests for materials should be addressed to Srijit Goswami.

Peer review information *Nature* thanks the anonymous reviewers for their contribution to the peer review of this work. Peer reviewer reports are available.

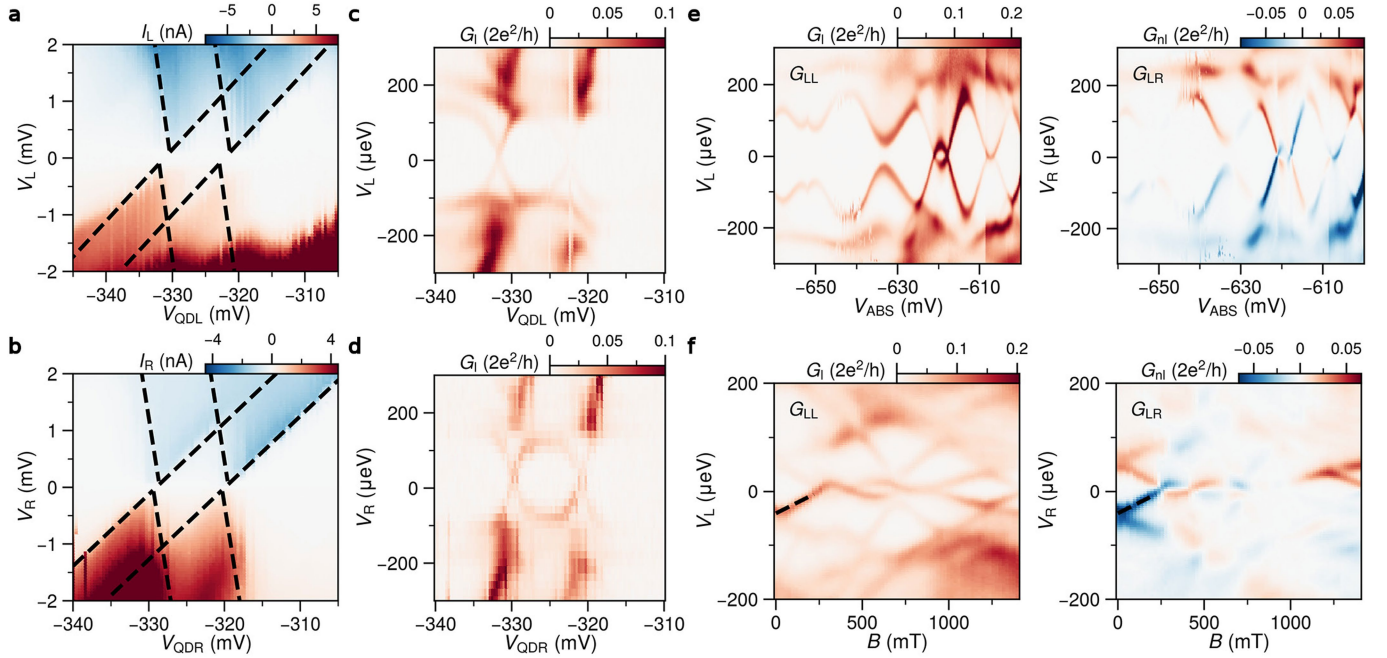

Extended Data Fig. 1 | Characterization of QDs and ABS spectroscopy for device A. a–**b**, Coulomb diamond measurements of the left and right QDs, in the regime used for measurements presented in Fig. 4. Charging energies are estimated to be 1.1 meV in each QD. The lever arm of the left and right dot is estimated to be $\alpha \approx 0.11$. **c**–**d**, Zoomed in views of figures (a) and (b) in a smaller energy range. Due to a large tunnel coupling between the QDs and the hybrid section, YSR-states form in the sub-gap spectrum of the QDs. Tunneling spectroscopy around the charge degeneracy points in (a-b) reveal clear sup-gap features within the Coulomb diamonds. As V_{QDL} and V_{QDR} are tuned, the sub-gap features form an eye-shape feature enclosing the doublet charge occupation. This behavior is typical for YSR-states with large charging energies[28]. **e**, Crossed Andreev reflection and elastic co-tunneling require the presence of extended ABSs. Local G_l and non-local conductance G_{nl} of the hybrid region are measured via tunnelling spectroscopy and their identical energy dependence as a function of V_{ABS} highlights that ABSs extend across the entire hybrid section. Comparable behavior was observed in a wide V_{ABS} range from 0 to −1 V. The measurement presented in Fig. 1 is taken at the V_{ABS} with the eye-shaped crossing. **f**, ABS spectroscopy as a function external magnetic field at $V_{ABS} = -623$ mV. The effect of splitting of the doublet state can be observed at low fields. A g-factor of 5.5 is extracted by linear fitting of the lowest sub-gap states (dashed line) in Extended Data Fig. 1d.

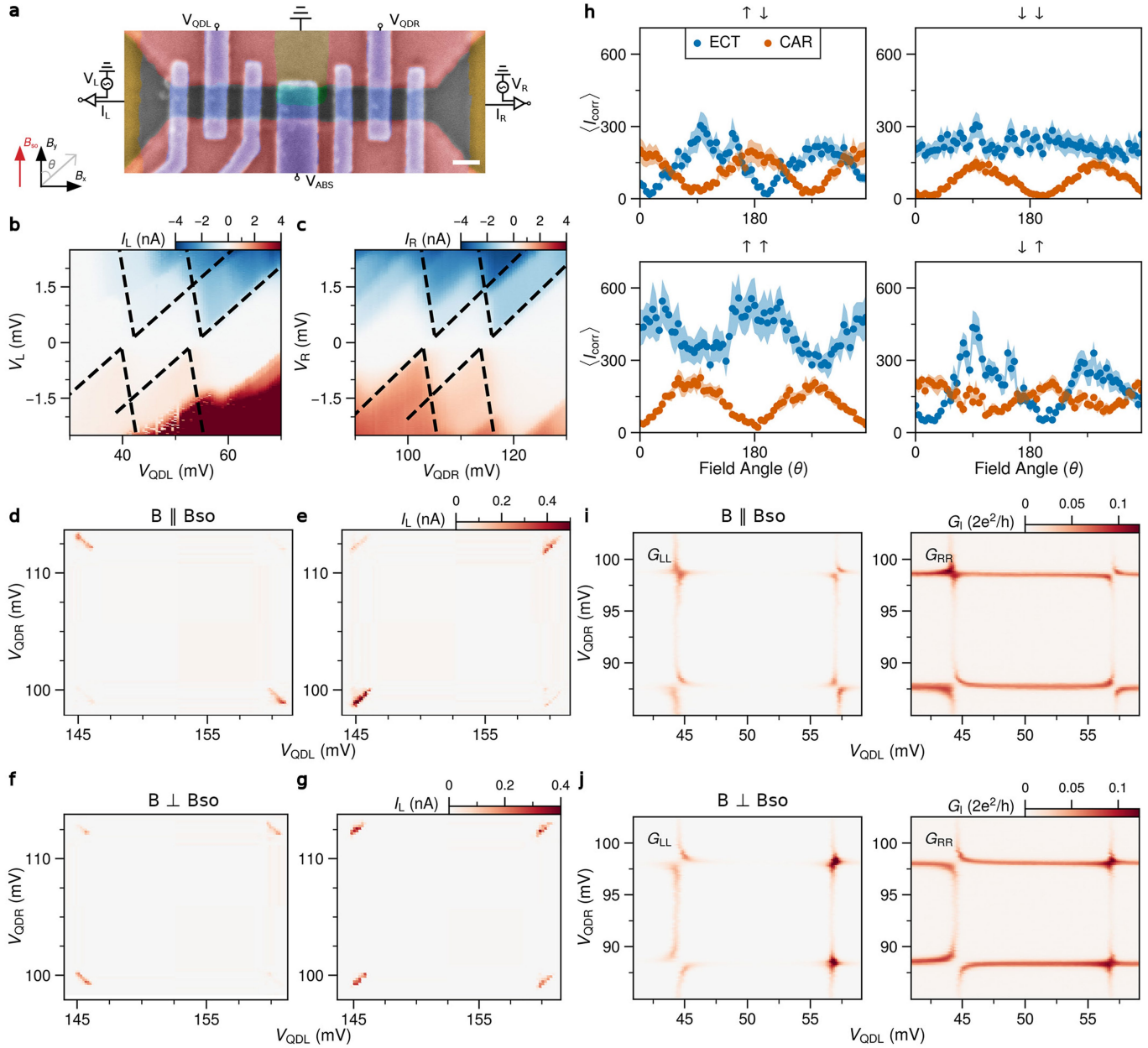

Extended Data Fig. 2 | Characterization of device B. a, Scanning electron micro-graph of device B, used to obtain the measurements presented in Fig. 2. Scale bar shown is 100 nm. **b**–**c**, Coulomb diamond measurements of the left and right QDs. Charging energies are extracted to be 1.4 meV. The lever arm α_N is extracted to be about 0.11 for each QD. This lever arm is used for the extraction in Fig. 2d. **d**–**e**, To validate the direction of B_{so} and to show the connection between interactions in strongly coupled QDs and underlying ECT and CAR processes, we first measure ECT and CAR currents in the weakly coupled dots, as detailed in[29]. With $B \perp B_{so}$, measurements of CAR (**d**) and ECT (**e**) show the typical blockades for same-spin and opposite-spin charge configurations respectively. In **f**–**g**, with $\mathbf{B} \| \mathbf{B}_{so}$, the spin non-conserving ECT and CAR processes are observed to be revived. **h**, Measuring CAR and ECT rates as a function of magnetic field angle θ shows the currents for the spin non-conserving processes are indeed smoothly controlled and become suppressed when $\theta = 0$. This supports the interpretation that $\mathbf{B} \| \mathbf{B}_{so}$ when $\mathbf{B}$ is perpendicular to the 1-D channel. **i**–**j**, Next, the QDs are operated with higher tunnelling rates between the QDs and the SC, to enable strong couplings. Similar to Fig. 1e-f, CSDs are obtained in the strongly interacting regime, taken with the verified $\mathbf{B} \| \mathbf{B}_{so}$ and $\mathbf{B} \perp \mathbf{B}_{so}$ respectively.

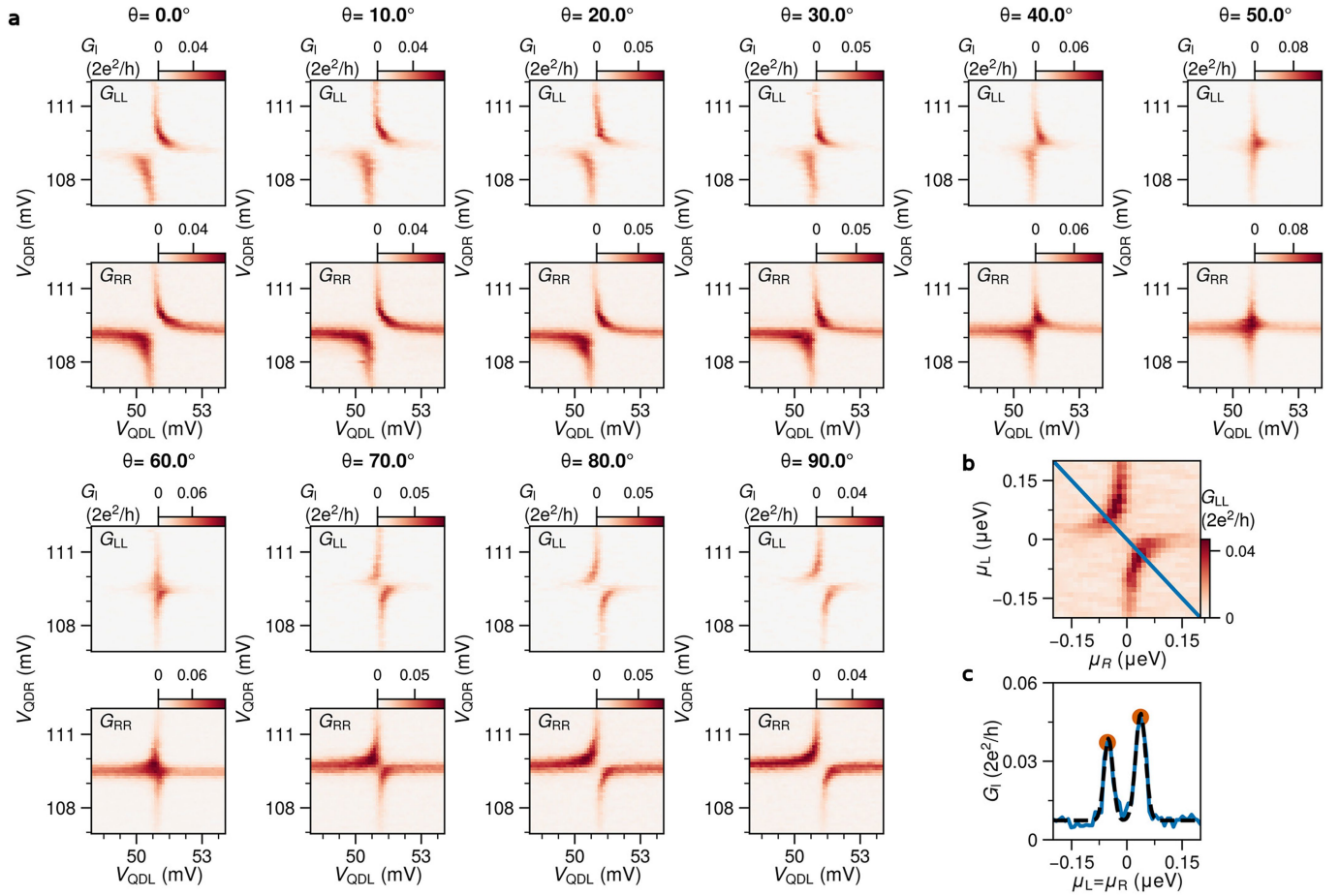

Extended Data Fig. 3 | Extended dataset of Fig. 2. a, CSDs measured at various magnetic field angles θ between 0° and 90°, used to extract the data shown in Fig. 2d. **b**, Example of the extraction process. For each obtained CSD, V_{QDL} and V_{QDR} are converted to energies μ_L and μ_R using lever arms obtained in Extended Data Fig. 2. Next, the conductance is extracted along a $\mu_L = -\mu_R$ or $\mu_L = \mu_R$ line. **c**, Two Gaussian peaks are fitted to extract the separation between the two avoided crossings, from which the quantity $\sqrt{|\Gamma_o - \Gamma_e|}$ is obtained (plotted in Fig. 2d).

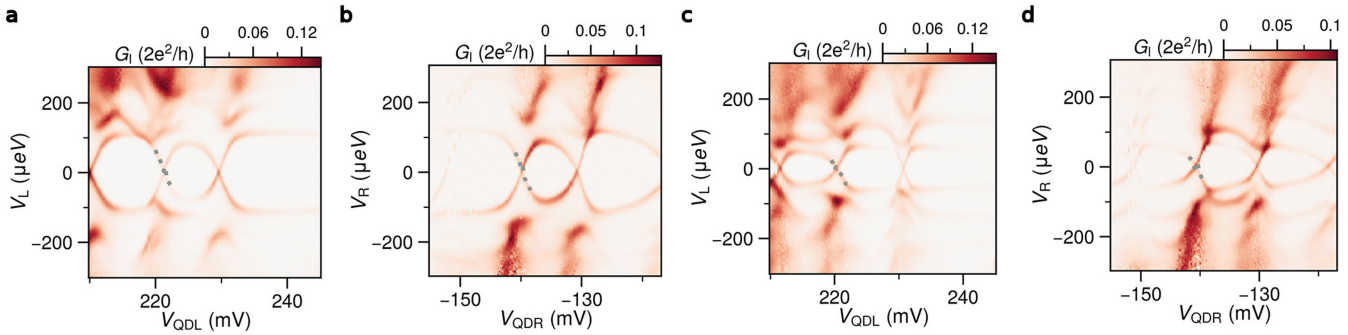

Extended Data Fig. 4 | Characterisation of YSR-states in QDs of Fig. 3. To complement the data in Fig. 3, Extended Data Fig. 5 and Extended Data Fig. 10, we measure the sub-gap states in QDL and QDR (see Extended Data Fig. 1). Using this, we obtain the lever arms of V_{QDL} and V_{QDR} on the YSR-state energies (denoted α_{YSR}) (see Methods). **a**–**b**, Sub-gap spectroscopy of QDL and QDR at $B_z = 0$ mT. From the slopes of the states upon crossing V_L, $V_R = 0$, we estimate $\alpha_{YSR} \approx 0.045$. Applying an external magnetic field lowers the energy of ABSs in the hybrid region, as a result of Zeeman splitting. This in turn will affect the YSR-spectrum of the QDs, due to increased hybridization between the QDs and the ABS. **c**–**d**, Measuring sub-gap spectroscopy of QDL and QDR at $B_z = 225$ mT for the same settings as in (a–b) shows indeed the effective lever arm here decreases to $\alpha_{YSR} \approx 0.028$.

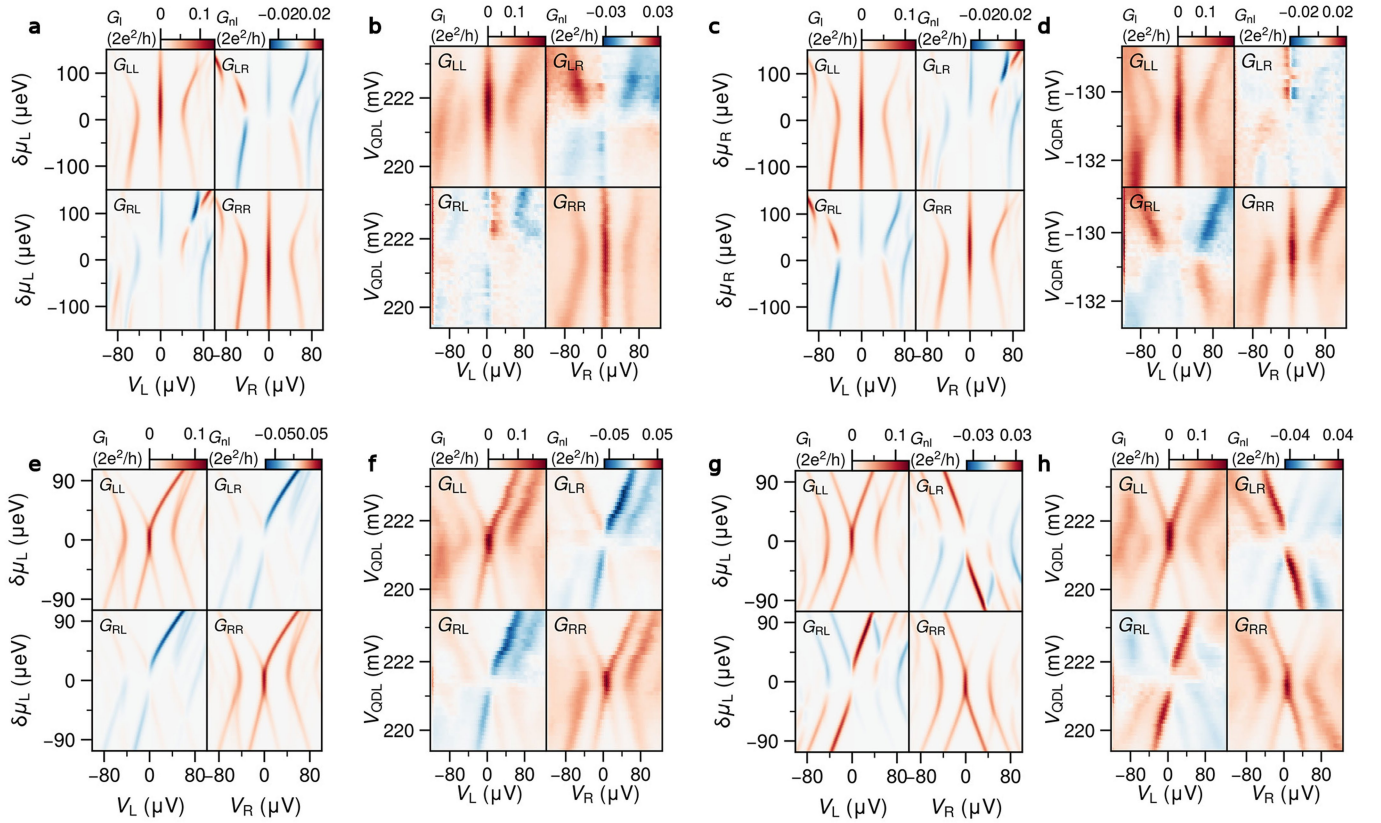

Extended Data Fig. 5 | Full conductance spectra at the sweet spot upon detuning V_{QDL} and V_{QDR}. A comparison between numerically calculated conductance and measured conductance in support of Fig. 3, measured at $B = 225$ mT. Presented results show the evolution of G_l and G_{nl} for four different cases: (**a**–**b**) detuning V_{QDL}, (**c**–**d**) detuning V_{QDR}, (**e**–**f**) detuning both V_{QDL} and V_{QDR} simultaneously along a diagonal path and (**g**–**h**) detuning both anti-diagonally. For each case, we find the behavior of both G_l and G_{nl} is well described by the numerical results.

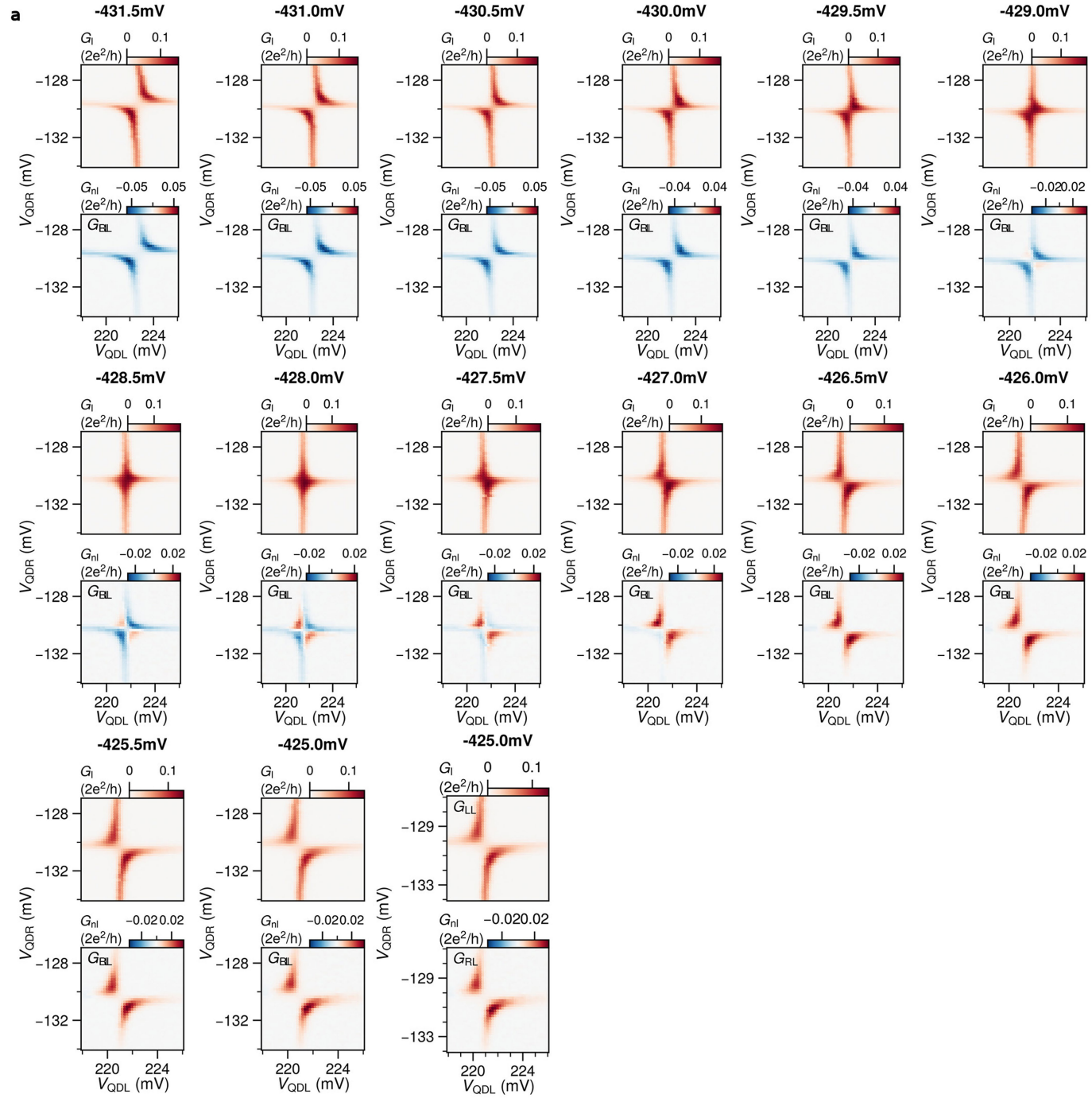

Extended Data Fig. 6 | Extended dataset for Fig. 3. a, Sets of CSDs obtained while varying V_{ABS} in the range presented in Fig. 3. The range of V_{QDL} and V_{QDR} is constant for each measurement. The slight drift of the avoided crossing upon varying V_{ABS} is owed to cross-capacitance between V_{ABS} and the potential of the QDs.

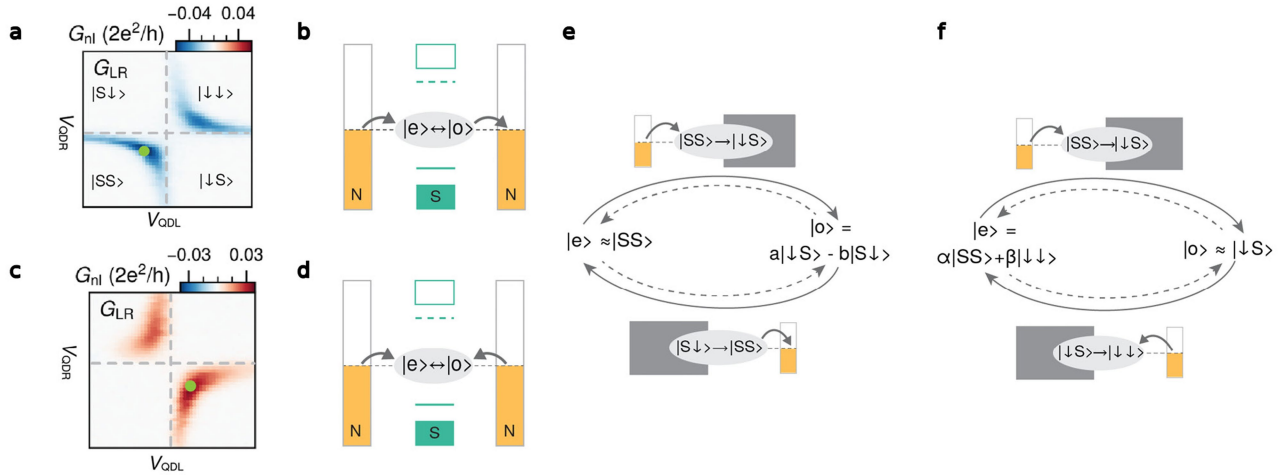

Extended Data Fig. 7 | Energy diagrams detailing non-local transport. In CSDs presented in Fig. 3, a clear sign change is observed when changing from the $\Gamma_O > \Gamma_E$ regime to the $\Gamma_O < \Gamma_E$ regime. This can be understood by considering the possible transport cycles that underlie the measured non-local conductance. **a**, When $\Gamma_O > \Gamma_E$, G_{nl} is observed to be negative in the measured CSDs (see Fig. 3c). **c**, When $\Gamma_O < \Gamma_E$, the same measurements yield a positive G_{nl} (see Fig. 3a). Horizontal and vertical dashed lines indicate $\mu_R = 0$ and $\mu_L = 0$ respectively. The state of the uncoupled system is labelled in each quadrant. **b,d**, In such CSD measurements, zero-bias transport can take place when the odd and even ground states are degenerate. For non-local transport to occur, the system can accept a hole/electron from one lead, and relax non-locally to its original state by either (**b**) donating a hole/electron to the opposite lead, giving rise to negative G_{nl}, or (**d**) accept a hole/electron from the opposite lead, giving rise to positive G_{nl}. The preferred path is dictated by the quadrant in μ_L, μ_R space where the odd-even degeneracy occurs. **e**, When $\mu_L, \mu_R > 0$ or $\mu_L, \mu_R < 0$, the former path is expected to dominate and the resulting G_{nl} will be negative. **f**, When $\mu_L > 0$ and $\mu_R < 0$ or vice versa, the latter path is expected to dominate and resulting G_{nl} will be positive.

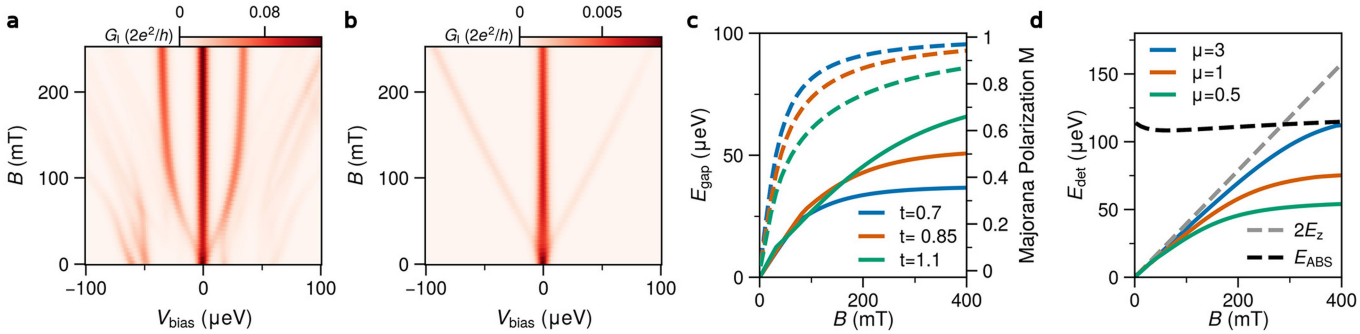

Extended Data Fig. 8 | Numerical analysis of E_{gap} and E_{det}. Numerical calculations supporting the results presented in Fig. 4. Through the procedure detailed in Methods, Majorana sweet spots are obtained and analysed for fields between 0 mT and 300 mT. **a**, Field evolution of G_{RR} line-traces at each sweet spot, showing the excitations above the ZBPs gradually increasing in energy and then saturating at ± 30 μeV. **b**, Field evolution of G_{RR} line-traces when QDR detuned by $3\Delta_{\mathrm{ind}}$, showing the excited states increase linearly in energy. From calculations in (a) and (b), E_{gap} and E_{det} are obtained, given by the energy between the lowest even-parity state and second-lowest odd-parity state. **c**, Extraction of E_{gap} (solid) and the Majorana polarization (dashed), for different values of the tunneling parameter t. In each case $t_{so} = 0.4t$. Larger tunnel coupling results in larger hybridization between ABSs, in turn lowering the MP at a specific magnetic field. **d**, Extraction of E_{det} for various values of detuning μ_{R}. In each case the slope at low fields corresponds to $2E_z$ (dashed grey line). The larger the detuning of μ_{R}, the longer this holds. The dashed black line shows the energy of the ABS E_{ABS}. At large detuning E_{det} will increase linearly with $2E_z$, until becoming of comparable E_{ABS} becomes the lowest energy scale.

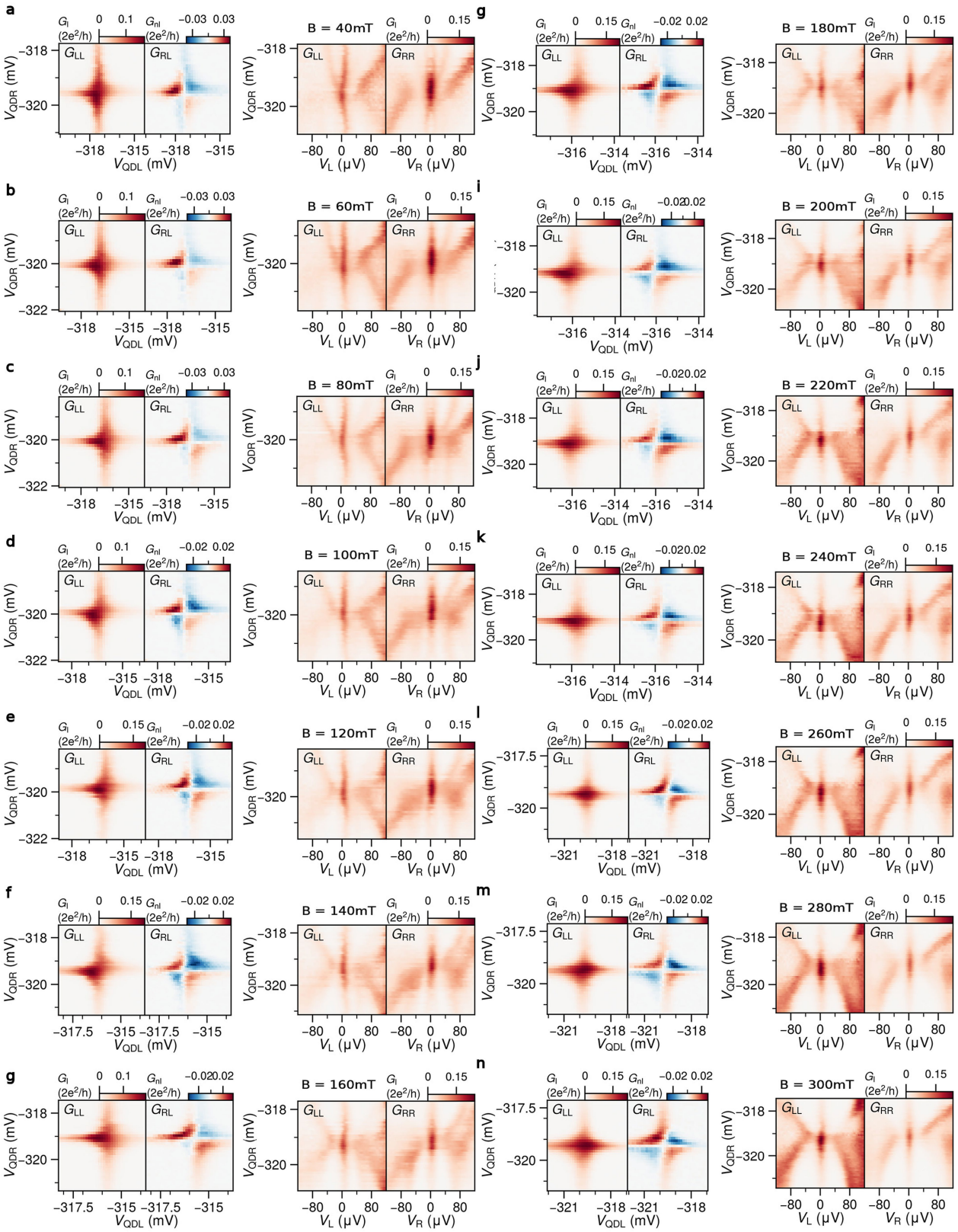

Extended Data Fig. 9 | Raw datasets for Fig. 4h. Obtained 'sweet spots' at magnetic fields between 0 mT and 300 mT. **a**–**i**, CSDs and tunnelling spectroscopy are measured at each sweet spot, where V_{QDR} is detuned. From these measurements E_{det} and E_{gap} are extracted, as described in the main text and in Methods.

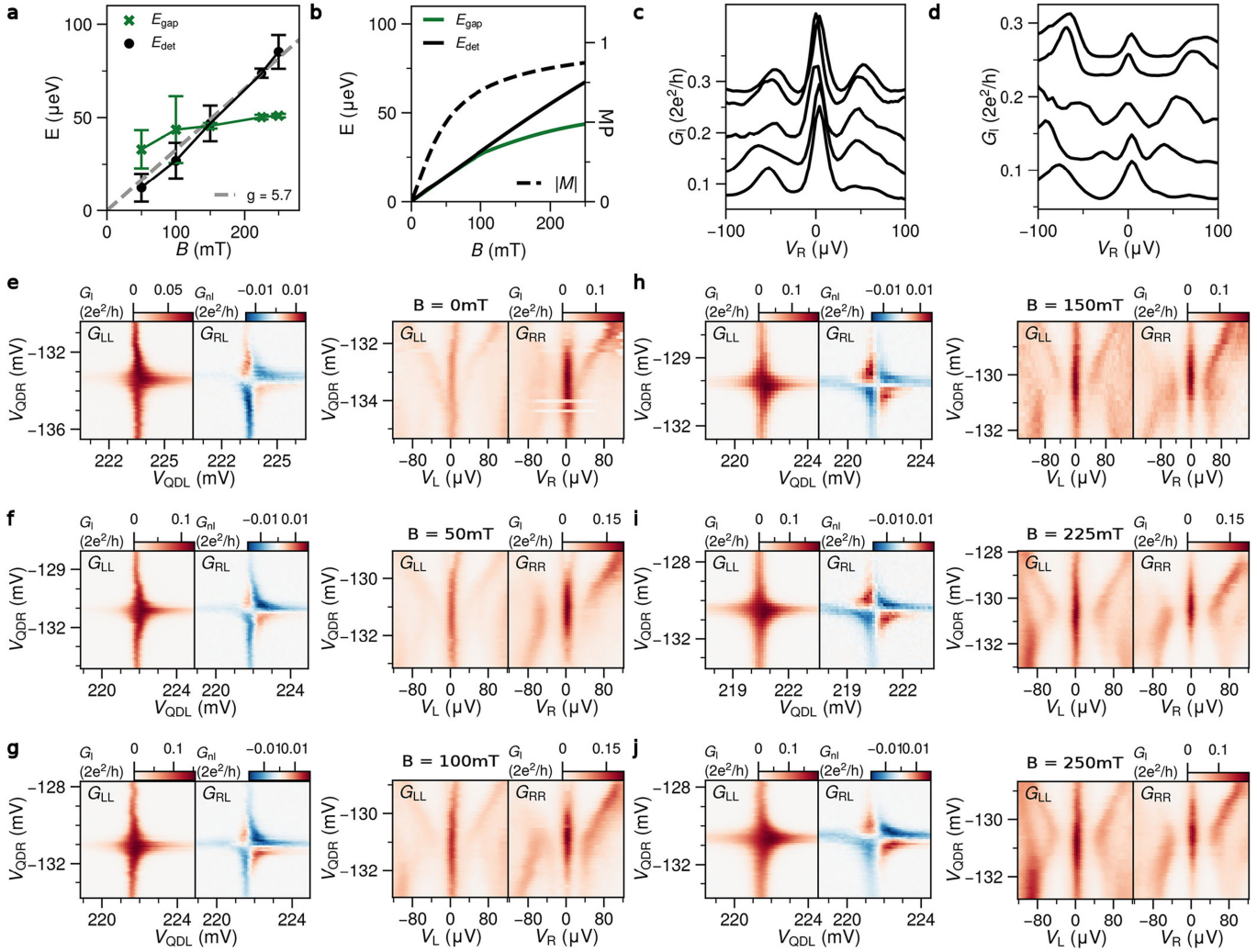

Extended Data Fig. 10 | Extended datasets supporting Fig. 4h. Reproduction of the main results from Fig. 4, using the orbitals shown in Fig. 3. Data was obtained at 6 different field values B between 0 and 250 mT. At each field V_{ABS} is adjusted to tune to the sweet spot. **a**, Extraction of E_{det} and E_{gap}, similar to the analysis presented in Fig. 4l. From a linear for of E_{det} a g-factor of 5.7 is estimated. **b**, Numerically obtained E_{det} and E_{gap}, using parameters tuned to compare to (**a**). At 250 mT, an estimate of $M \approx 0.9$ is obtained. Extrapolation for comparison to Fig. 4l yields $M \approx 0.92$ at 300 mT. **c**,**d**, Waterfall plots highlighting the line-traces used to extract the data in (**a**). **e**–**j**, Raw datasets of CSDs and tunnelling spectroscopy measurements, from which (a-d) is extracted. Datasets at 150 mT and 225 mT datasets are repeated from Fig. 3 and Extended Data Fig. 5 respectively.